High harmonic generation tomography of impurities in solids: Conceptual analysis

S. Almalki,[1,*] A. M. Parks,[1] G. Bart,[1] P. B. Corkum,[1,2] T. Brabec,[1] and C. R. McDonald[1,†]
[1]*Department of Physics, University of Ottawa, Ottawa, Ontario, Canada K1N 6N5*
[2]*National Research Council of Canada, Ottawa, Ontario, Canada K1A 0R6*

(Received 18 May 2018; published 24 October 2018)

A three-step model for high harmonic generation from impurities in solids is developed. The process is found to be similar to high harmonic generation in atomic and molecular gases, with the main difference coming from the nonparabolic nature of the bands. This opens a new avenue for strong-field atomic and molecular physics in the condensed-matter phase. As a first application, our conceptual study demonstrates the feasibility of tomographic measurement of impurity orbitals.

DOI: 10.1103/PhysRevB.98.144307

I. INTRODUCTION

Strong-field and attosecond science in atomic and molecular physics has made great strides over the past 20 years [1,2]. Strong laser-atom interaction takes place in a three-step process; first, the weakest bound electron is ionized, followed by laser-driven evolution in the continuum, and finally, it recollides/rescatters with its parent ion [1,3]. It has been found that both tunneling and recollision processes contain a great deal of information about the parent system's structure and dynamics.

Angular resolved tunnel ionization spectroscopy [4,5] reveals the orbital angular structure of the highest occupied molecular orbital.

When the electron recollides with its parent ion, recombination and rescattering take place. Recombination results in high harmonic generation (HHG), the emission of coherent XUV radiation. HHG has been used to time resolve chemical reactions and to tomographically measure the wave function of simple molecules [6–11].

Rescattering [12] results in nonsequential double ionization, above-threshold ionization, and laser-induced electron diffraction [13–16]; these processes have structural information encoded and are also promising candidates for time-resolved imaging of molecular reactions.

Recent experiments with midinfrared [17–20] and terahertz pump sources [21–23] have demonstrated HHG in solids. Theory has identified two mechanisms [24,25]: (i) intraband HHG due to the nonparabolic nature of bands [18] was found to be dominant in dielectrics; (ii) interband HHG dominates in semiconductors and is created in a three-step process similar to atomic and molecular HHG [26]. This similarity has established a connection between attosecond physics in atoms/molecules and in the condensed-matter phase.

Our analysis further deepens the links between strong-field physics in the gas and condensed-matter phases. Recently, HHG involving solid-state systems with impurities was considered [27,28]. In Ref. [27], a semiconductor material was doped by ion implantation to alter the band structure of the material; this ultimately led to enhanced harmonic emission under a mid-IR field. Here we will consider harmonic emission directly from the impurity under a terahertz driving field. We develop quantum equations of motion and a three-step model for this process. First, a free electron/hole is created in the conduction/valence band by tunnel ionization of a donor/acceptor impurity. Second, the electron/hole is accelerated by the laser field. In the third step a harmonic photon is emitted upon recollision and recombination with the parent impurity. Figure 1 depicts a schematic representation for HHG from shallow impurities in one dimension. In Fig. 1(a) we have the periodic potential of the unperturbed solid (blue line) plus a Coulomb potential from an impurity (red line). The shaded curve represents the ground state of the shallow impurity; this ground state extends over many lattice sites. The three-step model described above is shown in the real and reciprocal spaces in Figs. 1(b) and 1(c), respectively, for the system interacting with a strong laser field.

Besides differences in the continuum evolution due to the nonparabolic nature of bands, the process is found to be identical to HHG in gases. As a consequence, many of the above processes can be adapted from the gas to the condensed-matter phase. This opens a new research direction for atomic and molecular strong-field processes.

As a first application, we study the potential of applying molecular HHG tomography [9–11] to impurities. Tomographic reconstruction of the impurity ground state is demonstrated in a one-dimensional (1D) model system. The impurity dipole moment is found to be the dominant factor in determining the magnitude of the harmonic signal as a function of harmonic order; ionization and propagation, which have to be factored out in molecular tomography, play a lesser role here. This indicates substantial facilitation due to the potential for direct reconstruction of the impurity ground state from the harmonic spectrum.

Our results create a link between strong-field physics and solotronics, solitary impurity electronics; for a review see Ref. [29]. Solitary impurities are important building blocks for quantum technology, as qubits for quantum computing

*salma012@uottawa.ca
†cmcdo059@uottawa.ca

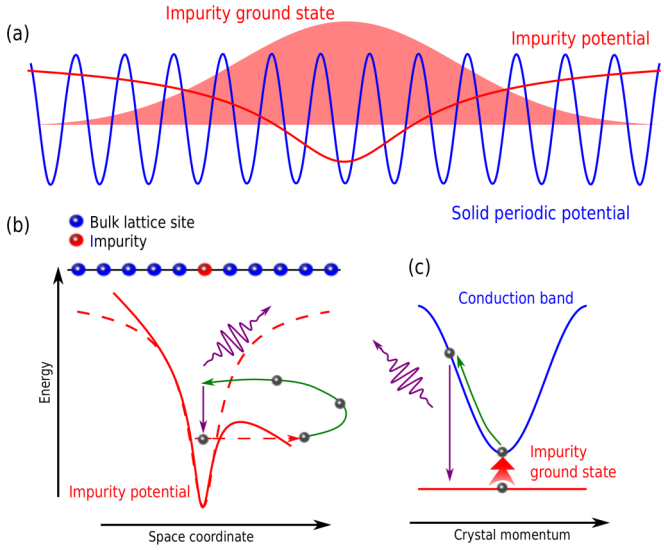

FIG. 1. (a) Periodic potential of the unperturbed bulk solid (blue) plus the impurity potential (red); the shallow impurity ground state that extends over many lattice sites is represented by the shaded curve. (b) Space representation of the three-step model for HHG from an impurity. (c) Reciprocal space representation of the three-step model for HHG from an impurity.

and as single-photon and nonclassical photon sources for quantum sensing and communication. Further, with increasing miniaturization, the device characteristics of metal-oxide-semiconductor field-effect transistors is strongly influenced by scattering off single impurities. All of the above applications require detailed knowledge about the wave function of impurity and environment. Currently, the most powerful method to image the wave function of single impurities is scanning tunneling microscopy close to suitably cleaved surfaces. Our results reveal that strong-field methods can offer complementary capacities. Among other things they provide an all-optical way to measure dipole moment and wave functions of impurity ensembles independent of surfaces; single-impurity imaging will be challenging due to the low quantum yield of HHG. Beyond that they open the path to spatiotemporal imaging of wave function dynamics in impurities, impurity molecules, and arrays [29] via optical pump-probe experiments.

This paper is structured as follows. In Sec. II we introduce the microscopic theory for an impurity-doped solid interacting with a strong laser field. We first introduce our quantum-mechanical model (Sec. II A) and then derive an approximate expression for the impurity ground state (Sec. II B). The equations of motion for the solution of the time-dependent Schrödinger equation are derived in Sec. II C; there we also produce an expression for the transition dipole between the impurity ground state and conduction band. Section II is ended with a derivation of the semiclassical equations (Sec. II D). In Sec. III we present the result from our numerical calculations. In Sec. III A we solve our equations of motion for a one-dimensional model system of a solid doped with an impurity and look at the harmonic spectrum and perform the semiclassical analysis. In Sec. III B we demonstrate a method for tomographic reconstruction of the impurity ground state. Finally, in Sec. III C we discuss dimensionality considerations for tomographic reconstruction.

II. THEORETICAL FRAMEWORK

A. Quantum-mechanical model

Our one-body analysis builds on, and extends, the theoretical work by Adams [30] and by Luttinger and Kohn [31,32]. To achieve this we use the following model: an impurity with potential $U(\mathbf{x})$ is embedded in a solid and is coupled to a laser field $\mathbf{F}(t)$ via the dipole coupling term $\mathbf{x}\cdot\mathbf{F}(t)$. The resulting time-dependent Schrödinger equation is given by

$$i\partial_t\Psi(\mathbf{x},t) = [H_i - \mathbf{x}\cdot\mathbf{F}(t)]\Psi(\mathbf{x},t), \tag{1}$$

where $H_i = H_0 + U(\mathbf{x})$ and $H_0 = \frac{1}{2}\mathbf{p}^2 + v(\mathrm{x})$ refers to the Hamiltonian of the solid without impurity, with $v(\mathrm{x})$ being the periodic lattice potential. Atomic units, $e = \hbar = m_e = 1$, are used throughout unless otherwise indicated. The eigenvalue equation of the field-free Hamiltonian H_i is given by

$$H_i\phi(\mathbf{x},t) = \varepsilon\phi(\mathbf{x},t). \tag{2}$$

In the absence of the impurity the eigenfunctions $\Phi_{m,\mathbf{k}}$ fulfill $H_0\Phi_{m,\mathbf{k}} = E_m(\mathbf{k})\Phi_{m,\mathbf{k}}$, with m being the band index and $E_m(\mathbf{k})$ being the band eigenenergies. Further, the eigenfunctions are given by

$$\Phi_{m,\mathbf{k}}(\mathbf{x}) = \frac{1}{\sqrt{V}}u_{m,\mathbf{k}}(\mathbf{x})e^{i\mathbf{k}\cdot\mathbf{x}}, \tag{3}$$

where $u_{m,\mathbf{k}}$ is the Bloch function that is periodic with the lattice and V is the volume of the solid. The unit cell is defined by basis vectors $\mathbf{a}_l$ ($l = 1, 2, 3$) and volume υ; $\mathbf{R}_n = \sum_l n_l\mathbf{a}_l$ is a lattice vector that connects two identical sites in the lattice. The crystal momentum $\mathbf{k}$ extends over the first Brillouin zone (BZ) defined as the Wigner-Seitz cell of the reciprocal lattice whose primitive vectors $\mathbf{b}_l$ are determined through $\mathbf{b}_l\cdot\mathbf{a}_j = 2\pi\delta_{lj}$; we denote the magnitude of the reciprocal lattice vector $\mathbf{b}_l$ as $b_l = |\mathbf{b}_l|$. The vectors of the reciprocal lattice are given by $\mathbf{K}_n = \sum_l n_l\mathbf{b}_l$. The eigenfunctions are orthonormalized according to

$$\int_V \Phi^*_{m',\mathbf{k}'}\Phi_{m,\mathbf{k}}d\mathbf{x} = \delta_{mm'}\delta(\mathbf{k}-\mathbf{k}'). \tag{4}$$

By defining $V = N\upsilon$, with N being the number of atomic unit cells, we obtain from the orthonormality relation $\int_\upsilon |u_{m,\mathbf{k}}|^2 d\mathbf{x} = \upsilon$.

Shallow donor (acceptor) impurities split into an electron (hole) and a positively (negatively) charged residual ion; the electron (hole) moves in the lowest conduction (highest valence) band and has bound states in the field of the residual ion with energies closely below (above) the bottom (top) of the conduction (valence) band. As a result, we drop the band index m and confine our treatment to a single band with eigenfunctions $\Phi_\mathbf{k}$ which fulfill $H_0\Phi_\mathbf{k} = E(\mathbf{k})\Phi_\mathbf{k}$, with $E(\mathbf{k})$ being the band eigenenergies. Further, we consider a single impurity level (the impurity ground state) with eigenenergy ε_0 and eigenfunction ϕ_0; here Eq. (2) reads

$$H_i\phi_0(\mathbf{x}) = \varepsilon_0\phi_0(\mathbf{x}). \tag{5}$$

As this is a conceptual study we have limited ourselves to only the most fundamental process and confined our system to only

the ground state. Additional complexity can be added to the model by including excited states of the impurity potential.

B. Derivation of the ground state for a shallow impurity

Equation (5) is solved by expanding the eigenstate ϕ_0 in terms of Bloch states,

$$\phi_0(\mathbf{x}) = \int_{\mathrm{BZ}} b_0(\mathbf{k})\Phi_{\mathbf{k}}(\mathbf{x})d\mathbf{k}. \tag{6}$$

Inserting Eq. (6) into Eq. (5), multiplying the result by $\Phi^*_{\mathbf{k}'}(\mathbf{x})$, and integrating over the spatial coordinate yield

$$[E(\mathbf{k}) - \varepsilon_0]b_0(\mathbf{k}) + \int_{BZ} \widetilde{U}(\mathbf{k},\mathbf{k}')b_0(\mathbf{k}')d\mathbf{k}' = 0, \tag{7}$$

with

$$\widetilde{U}(\mathbf{k},\mathbf{k}') = \int_V u^*_{\mathbf{k}}(\mathbf{x})u_{\mathbf{k}'}(\mathbf{x})U(\mathbf{x})e^{i(\mathbf{k}'-\mathbf{k})\cdot\mathbf{x}}d\mathbf{x}, \tag{8}$$

where integration is performed over the crystal volume V. By noting that $u_{\mathbf{k}}$ is periodic with the unit cell, the Bloch functions in Eq. (8) can be expanded in a Fourier series,

$$u^*_{\mathbf{k}}(\mathbf{x})u_{\mathbf{k}'}(\mathbf{x}) = \frac{1}{\sqrt{\upsilon}}\sum_n M^{(n)}_{\mathbf{k},\mathbf{k}'}e^{-i\mathbf{K}_n\cdot\mathbf{x}}, \tag{9}$$

with

$$M^{(n)}_{\mathbf{k},\mathbf{k}'} = \frac{1}{\sqrt{\upsilon}}\int_{\upsilon} u^*_{\mathbf{k}}(\mathbf{x})u_{\mathbf{k}'}(\mathbf{x})e^{i\mathbf{K}_n\cdot\mathbf{x}}d\mathbf{x}. \tag{10}$$

As a result, we obtain for the Coulomb matrix element

$$\widetilde{U}(\mathbf{k},\mathbf{k}') = \sum_n M^{(n)}_{\mathbf{k},\mathbf{k}'}\int_{\upsilon} U(\mathbf{x})e^{i(\mathbf{k}'-\mathbf{k}-\mathbf{K}_n)\cdot\mathbf{x}}d\mathbf{x}. \tag{11}$$

By inserting the series expansion (9) into the orthonormality relation for the Bloch eigenfunction (4) we obtain the relation

$$\frac{1}{\sqrt{\upsilon}}\int_{\upsilon} M^{(0)}_{\mathbf{k},\mathbf{k}'}e^{i(\mathbf{k}-\mathbf{k}')\cdot\mathbf{x}}d\mathbf{x} = \delta(\mathbf{k}-\mathbf{k}'). \tag{12}$$

Note that expansion terms with $n \neq 0$ result in $\delta(\mathbf{k}-\mathbf{k}'-\mathbf{K}_n) = 0$ as $\mathbf{k}, \mathbf{k}'$ are from the first BZ. Equation (12) yields

$$M^{(0)}_{\mathbf{k},\mathbf{k}'} = \frac{\sqrt{\upsilon}}{(2\pi)^3}. \tag{13}$$

For a soft potential whose main components correspond to wavelengths that are much smaller than the lattice spacing, $|\mathbf{k}-\mathbf{k}'| \ll b_l$, the lowest-order Fourier term dominates, and we obtain [30,31]

$$\widetilde{U}(\mathbf{k}-\mathbf{k}') \approx \frac{\sqrt{\upsilon}}{(2\pi)^3}\int_{\upsilon} U(\mathbf{x})e^{i(\mathbf{k}'-\mathbf{k})\cdot\mathbf{x}}d\mathbf{x}, \tag{14}$$

where we have written $\widetilde{U}(\mathbf{k},\mathbf{k}')$ as $\widetilde{U}(\mathbf{k}-\mathbf{k}')$ to indicate that the argument in $\widetilde{U}$ of our approximate expression above depends only on the difference $\mathbf{k}-\mathbf{k}'$. Note that close to the Coulomb singularity this assumption is violated, and higher-order Fourier terms need to be included. Inserting Eq. (14) in Eq. (7) yields

$$[E(\mathbf{k}) - \varepsilon_0]b_0(\mathbf{k}) + \int_{BZ} \widetilde{U}(\mathbf{k}-\mathbf{k}')b_0(\mathbf{k}')d\mathbf{k}' = 0. \tag{15}$$

For the sake of simplicity we focus here on direct band gap materials; however, the theory can be easily generalized to indirect semiconductors following the treatment in Refs. [31,32]. By invoking again the assumption that the potential is soft and couples only components $|\mathbf{k}-\mathbf{k}'| \ll b_l$, we can further simplify Eq. (15). The bound states extend over many unit cells corresponding to a narrow band of crystal momenta $b(\mathbf{k})$ centered about the Γ point ($\mathbf{k} = 0$). In real space this corresponds to a slowly varying modulation that is superimposed onto the Bloch eigenfunction,

$$B_0(\mathbf{x}) = \int_{BZ} b_0(\mathbf{k})\exp(i\mathbf{k}\cdot\mathbf{x})d\mathbf{k}. \tag{16}$$

As a result of the narrow width of $b(\mathbf{k})$ the conduction band can be Taylor expanded, which yields

$$E(\mathbf{k}) \approx E_g + \sum_{i,j}\frac{1}{2}\beta_{ij}k_ik_j, \tag{17}$$

where $i, j = x, y, z$ and $\beta_{ij} = \partial_{k_i}\partial_{k_j}E$ is the inverse mass tensor that arises from the quadratic expansion of the band energy $E(\mathbf{k})$ about the Γ point ($\mathbf{k} = 0$), where the band energy $E(\mathbf{k}=0) = E_g$ is minimum. For the sake of simplicity we confine our analysis to direct band gap materials; a generalization to indirect bands can be done by following the treatment in Ref. [32].

Using Eqs. (16) and (17), in Eq. (15) we obtain an atomiclike Schrödinger equation for the impurity eigenstates

$$\left[\frac{1}{2}\sum_{i,j}\beta_{ij}\nabla_i\nabla_j - U(\mathbf{x}) + (\varepsilon_0 - E_g)\right]B_0(\mathbf{x}) = 0. \tag{18}$$

Diagonalization of Eq. (18) yields ground-state wave functions $B_0(\mathbf{x})$ and $b_0(\mathbf{k})$ in k space. Its eigenenergy ε_0 determines the ionization potential as $\varepsilon_0 - E_g$. The complete impurity ground state is determined by inserting $b_0(\mathbf{k})$ into Eq. (6), which results in

$$\phi_0(\mathbf{x}) = \int_{\mathrm{BZ}} b_0(\mathbf{k})\Phi_{\mathbf{k}}(\mathbf{x})d\mathbf{k} \approx \Phi_{\mathbf{k}=0}(\mathbf{x})B_0(\mathbf{x}). \tag{19}$$

In the last step we have used $\Phi_{\mathbf{k}}(\mathbf{x}) \approx u_{\mathbf{k}=0}(\mathbf{x})\exp(i\mathbf{k}\cdot\mathbf{x})$, a result from the $\mathbf{k}\cdot\mathbf{p}$ perturbation theory.

C. Solution of the time-dependent Schrödinger equation

The solution of the time-dependent Schrödinger equation (1) in the presence of a strong laser field is developed along the lines of strong-field atomic physics [3,33]. The wave function is split into a bound-state part and a band contribution by using the ansatz

$$\Psi(\mathbf{x},t) = \phi_0(\mathbf{x}) + \int_{\mathrm{BZ}} a(\mathbf{k},t)\Phi_{\mathbf{k}}(\mathbf{x})d\mathbf{k}, \tag{20}$$

where the integral runs over the first BZ. We assume, in the spirit of the strong-field approximation [3], that field-induced ionization is weak enough that the ground-state population remains unaffected. This amounts to neglecting the dynamic Stark shift of the impurity ground state.

Inserting Eq. (20) into Eq. (1) and multiplying the resulting equation by the functional $\langle\Phi_{\mathbf{k}'}(\mathbf{x})|$, we obtain

$$i\frac{d}{dt}a(\mathbf{k},t) = [E(\mathbf{k}) - \varepsilon_0 + i\mathbf{F}(t)\cdot\nabla_{\mathbf{k}}]a(\mathbf{k},t) + \int_{BZ} U(\mathbf{k}-\mathbf{k}')a(\mathbf{k}',t)d\mathbf{k}' + i\mathbf{d}_0(\mathbf{k})\cdot\mathbf{F}(t), \tag{21}$$

where the transition dipole moment between the impurity ground state and conduction band is

$$\mathbf{d}_0(\mathbf{k}) = \int_V \Phi^*_{\mathbf{k}'}(\mathbf{x})\mathbf{x}\phi_0(\mathbf{x})d\mathbf{x}. \tag{22}$$

Equation (21) is similar to the equation of atomic strong-field physics [3]. Around the Γ point, where the effective-mass approximation is valid, Eq. (21) becomes identical to the equation for atomic gases. We note, however, that in Eq. (21) the full band is used and not the effective-mass approximated band in Eq. (17).

Here we have again employed the assumptions used for the derivation of the impurity potential matrix element (14) where a soft impurity potential is assumed for which large momentum scattering $|\mathbf{k}| > |\mathbf{b}_l|$ is negligible. In terms of dynamical processes, these assumptions amount to neglecting large-angle scattering events of the order of or larger than the inverse lattice vectors, which occur when a slow electron comes close to the Coulomb singularity and undergoes scattering. Further, the resulting intraband dipole matrix element is well defined only when written as [25]

$$\int_V \Phi^*_{\mathbf{k}'}(\mathbf{x})\mathbf{x}\Phi_{\mathbf{k}}(\mathbf{x})d\mathbf{x} = -i\nabla_{\mathbf{k}} + \mathbf{d}_c(\mathbf{k}), \tag{23}$$

where

$$\mathbf{d}_c = -i\int_V \Phi_{\mathbf{k}'}(\mathbf{x})\nabla_{\mathbf{k}}\Phi_{\mathbf{k}}(\mathbf{x})d\mathbf{x}. \tag{24}$$

We assume here inversion-symmetric materials for which $\mathbf{d}_c = 0$. As long as the impurity ground state and conduction band wave function vary slowly compared to the Bloch functions, the dipole moment between the impurity ground state and conduction band is given by

$$\mathbf{d}_0(\mathbf{k}) \approx \frac{1}{(2\pi)^3}\int_V \mathbf{x}B_0(\mathbf{x})e^{-i\mathbf{k}\cdot\mathbf{x}}d\mathbf{x}. \tag{25}$$

Here we have again applied Eq. (13) to approximately eliminate the product of Bloch functions. We find that the dipole moment is proportional to the Fourier transform of the atom-like part of the impurity ground state, just as in the atomic strong-field model. Finally, agreement with atomic strong-field physics becomes complete when the quadratic mass approximation is applied to Eq. (21) [3,33].

In the strong-field limit, the Coulomb potential in Eq. (21) is neglected. For impurities additional justification comes from the fact that photoionization cross sections are well described by replacing the Coulomb with δ-function potentials [34,35]. Integration of the resulting equation (21) and inserting the result into the second term of Eq. (6) yields the time-dependent evolution of the electron wave function in the conduction band as

$$a(\mathbf{k},t) = \int_{-\infty}^{t} dt'\mathbf{d}_0(\boldsymbol{\kappa}_{t'})\cdot\mathbf{F}(t')e^{\int_{-\infty}^{t'} i[\varepsilon_0 - E(\boldsymbol{\kappa}_{t''}) + \frac{i}{T_2}]dt''}, \tag{26}$$

where $\boldsymbol{\kappa}_{t'} = \mathbf{k} - \mathbf{A}(t) + \mathbf{A}(t')$, with vector potential determined by $\mathbf{F} = -d\mathbf{A}/dt$; further, a phenomenological dephasing time T_2 has been added.

Finally, high harmonic generation is determined by the current

$$\mathbf{j}(t) = \frac{d}{dt}\int_V \mathbf{x}|\Psi(\mathbf{x},t)|^2 d\mathbf{x} = \frac{d}{dt}\int_{\mathrm{BZ}} a(\mathbf{k},t)\mathbf{d}_0^*(\mathbf{k})d\mathbf{k} + \int_{\mathrm{BZ}}\Big[a^*(\mathbf{k}',t)a(\mathbf{k},t) \times \frac{1}{i}\int_V \Phi^*_{\mathbf{k}'}(\mathbf{x})\nabla\Phi_{\mathbf{k}}(\mathbf{x})d\mathbf{x}\Big]d\mathbf{k}'d\mathbf{k} + \mathrm{c.c.} \tag{27}$$

The second term in Eq. (27), corresponding to the intraband current, comes as a result of changing the Schrödinger picture to the Heisenberg picture, using $d\mathbf{x}/dt = \mathbf{p}$ and then converting back to the Schrödinger picture. Further simplification can be made using the relation

$$\frac{1}{i}\int_V \Phi^*_{\mathbf{k}'}(\mathbf{x})\nabla\Phi_{\mathbf{k}}(\mathbf{x})d\mathbf{x} = \nabla_{\mathbf{k}}E(\mathbf{k})\delta(\mathbf{k}-\mathbf{k}'), \tag{28}$$

with $\mathbf{v}(\mathbf{k}) = \nabla_{\mathbf{k}}E(\mathbf{k})$ being the band velocity [36]. We then obtain

$$\mathbf{j}(t) = \mathbf{j}_i(t) + \mathbf{j}_{ra}(t), \tag{29}$$

where

$$\mathbf{j}_i(t) = \frac{d}{dt}\int_{\mathrm{BZ}} a(\mathbf{k},t)\mathbf{d}_0^*(\mathbf{k})d\mathbf{k} + \mathrm{c.c.} \tag{30}$$

is the current due to the polarization buildup between the band electron and impurity and

$$\mathbf{j}_{ra}(t) = \int_{\mathrm{BZ}} |a(\mathbf{k},t)|^2\mathbf{v}(\mathbf{k})d\mathbf{k} + \mathrm{c.c.} \tag{31}$$

is the intraband current arising from the laser-driven motion of the electron in the band; this contribution comes from the nonparabolicity of the band and is not present in HHG from atomic gases.

D. Semiclassical model for impurity high harmonic generation

The high harmonic electric fields are determined by the polarization buildup between the band and impurity ground state, resulting in a current

$$\tilde{j}_i(\omega) = i\omega\int_{\mathrm{BZ}} d\mathbf{k}\,\mathbf{d}_0^*(\mathbf{k})\int_{-\infty}^{\infty} dt e^{-i\omega t}\int_{-\infty}^{t} dt'\mathbf{d}_0(\boldsymbol{\kappa}_{t'})\cdot\mathbf{F}(t') \times e^{[iS(\mathbf{k},t',t) - \frac{1}{T_2}(t-t')]dt''} + \mathrm{c.c.}, \tag{32}$$

where $S(\mathbf{k},t',t) = \int_t^t[\varepsilon_0 - E(\boldsymbol{\kappa}_{t''})]dt''$.

The three integrals in Eq. (32) can be solved analytically by the saddle point method [3]. The saddle point equations are determined by

$$\nabla_{\mathbf{k}}S = \int_{t'}^{t}\mathbf{v}(\boldsymbol{\kappa}_{t''})dt'' = \mathbf{x}(t) - \mathbf{x}(t') = 0, \tag{33a}$$

$$\frac{dS}{dt'} = E[\mathbf{k} - \mathbf{A}(t) + \mathbf{A}(t')] - \varepsilon_0 = 0, \tag{33b}$$

$$\frac{dS}{dt} = E(\mathbf{k}) - \varepsilon_0 = \omega. \tag{33c}$$

In Eq. (33a), the band velocity is given by $\mathbf{v}(\mathbf{k}) = \nabla_{\mathbf{k}} E$. This equation states that HHG can take place only when the electron, born at time t' in the band, returns to the parent impurity at t. Equation (33b) states that electrons are born with zero momentum at time t', $\mathbf{k} = \mathbf{A}(t = t') - \mathbf{A}(t') = 0$. At the time of recombination t the electron crystal momentum is given by $\mathbf{k}(t', t) = \mathbf{A}(t) - \mathbf{A}(t')$. The finite impurity gap energy results in a complex birth time, which is responsible for tunnel ionization. Finally, Eq. (33c) represents conservation of energy: the electron recombines to the ground state and emits a photon ω with energy equal $E(\mathbf{k}(\mathbf{t}', \mathbf{t})) - \varepsilon_0$. Again, at moderate laser intensities, for which the effective-mass approximation applies, the saddle point equations for the atom and impurity become identical.

After saddle point integration we obtain for the harmonic intensity

$$|\tilde{j}_i(\omega)|^2 = \left| \sum_{t'} \sqrt{w(t')} \mathbf{d}_0^*(\mathbf{k}) \alpha(t', t) e^{\int_{t'}^{t} (i\mathcal{S} - \frac{1}{T_2}) dt''} \right|^2, \quad (34)$$

where $\mathcal{S} = \varepsilon_0 + \omega - E(\mathbf{k}(t'', t))$, w$(t')$ is the ionization rate, and $t'(t(\omega))$ and $t(\omega)$ are birth and recombination times resulting in the generation of a harmonic with frequency ω. For an isotropic lattice the ionization rate is determined by the Ammosov-Delone-Krainov (ADK) tunnel ionization rate of atoms [4] with the electron mass replaced by the effective mass. Further, the dipole moment represents the recombination amplitude; the remaining term α in the preexponential is the propagation amplitude accounting for quantum diffusion and dephasing; this depends on the band specifics. For isotropic materials in the effective-mass m approximation $\alpha \propto m \exp[-(t - t')/T_2](t - t')^{-3/2}$. The main difference between HHG from impurities and atoms arises from the finite, nonparabolic, anisotropic nature of the bands.

III. RESULTS AND DISCUSSION

In the remaining part we use the above formalism to investigate HHG and the tomographic reconstruction of the impurity ground-state wave function from harmonic spectra.

A. Numerical details

For the analysis of HHG tomography of impurities we use a 1D model system for a direct band gap semiconductor. The periodic lattice potential is composed of lattice cells with width $a = 9.45$ a.u. $= 5$ Å and well depth $v_0 = 0.55$ a.u. $=$ 15 eV. The lattice cells are separated by a mollifier function [37]; the lattice cell centered at $x = 0$ is given by

$$v(x) = \begin{cases} v_0 e^{-\frac{(x+a/2)^2}{\sigma^2 - (x+a/2)^2}} - v_0 & \text{for } -\frac{a}{2} \leqslant x < -\frac{a}{2} + \sigma, \\ v_0 e^{-\frac{(x-a/2)^2}{\sigma^2 - (x-a/2)^2}} - v_0 & \text{for } \frac{a}{2} - \sigma < x \leqslant \frac{a}{2}, \\ -v_0 & \text{otherwise,} \end{cases} \quad (35)$$

where σ represents the extension of the mollifier. Each cell is represented on a space grid of 40 points, giving a grid spacing of $\Delta x = 0.236$. We use 400 cells to the left and right of the central cell for a total of 801 cells. The Coulomb potential is centered over the central cell and is given by

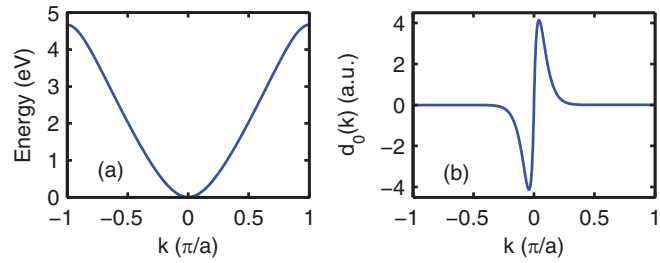

FIG. 2. (a) Structure of the conduction band obtained from diagonalization of the Hamiltonian. (b) Dipole moment calculated using Eq. (22).

$$U(x) = \frac{-1}{\epsilon\sqrt{x^2 + s^2}}, \quad (36)$$

where s is the softening parameter and ϵ is the dielectric constant. For our model we use $s = 25$ a.u. and $\epsilon = 5$ a.u.

The Hamiltonian is diagonalized using periodic boundary conditions in both the presence and absence of the Coulomb potential. In the absence of the Coulomb potential we obtain the Bloch functions $\Phi_k(x)$; the energy gap between the highest valence band and lowest conduction band at the Γ point is approximately 4 eV. When the Coulomb potential is present, we obtain the impurity ground state; for this system the impurity ground state lies at an energy of 106.4 meV below the Γ point of the conduction band. Figure 2(a) shows the calculated conduction band versus the crystal momentum k. In Fig. 2(b) the dipole moment calculated from Eq. (25) is shown.

The system is irradiated by a laser field with vector potential $A(t) = -(F_0/\omega_0) f(t) \sin(\omega_0 t)$ with peak field strength F_0 and center frequency ω_0. The peak field strength is $F_0 = 1 \times 10^{-4}$ a.u., which corresponds to a peak intensity of $I_0 = 3.5 \times 10^8$ W/cm^2 in the material. For the center frequency we use $\omega_0 = 9.1 \times 10^{-4}$ a.u.; this corresponds to a wavelength of $\lambda_0 = 50\,\mu$m. The pulse has a Gaussian envelope $f(t)$ with a FWHM of $12T_0$; here $T_0 = 2\pi/\omega_0 = 166$ fs. The time dynamics of the system are determined from Eq. (26) with $T_2 = 50$ fs. The dephasing time T_2 is chosen such that it is similar to dephasing times in semiconductors [38–40].

The parameters of our laser pulse and model system result in a minimum $n = 5$ photon transition from the impurity ground state to the conduction band using a pulse with an intensity of the order of 10^8 W/cm^2. For comparison ZnO has a Γ-point energy of 3.3 eV between the highest valence and lowest conduction bands; doping with impurities such as H, Ga, Al, and In leads to impurity donor states in the range 46–73 meV [41]. For a similar $n = 5$ photon transition, such a system would require a laser pulse with a central wavelength of ∼100 μm with an intensity of ∼100 MW/cm^2, which is achievable [42]. By contrast ZnSe has a band gap of 2.8 eV with a donor level 1.2 eV below the bottom of the conduction band when doped with V [43]. Thus, the parameters chosen here give a reasonable approximation to a semiconductor with shallow donor impurity levels.

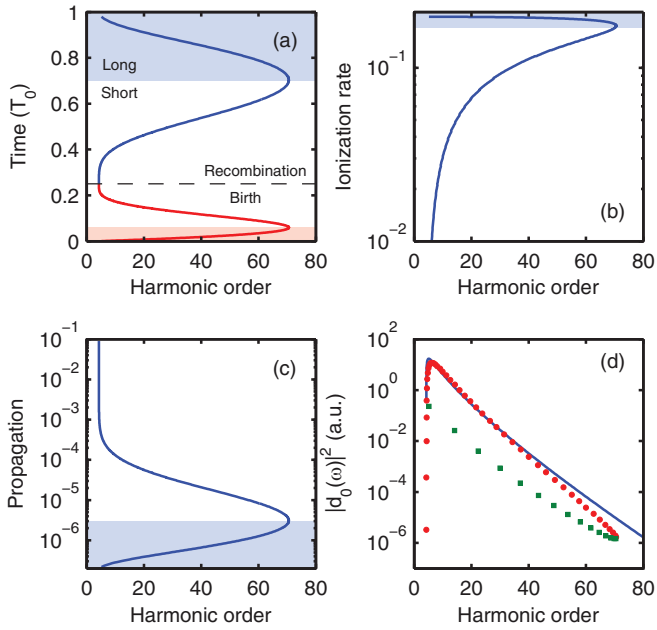

FIG. 3. (a) Birth time t' (red) and return times t (blue) from the semiclassical trajectories versus harmonic order. (b) Ionization rate $w \propto \exp\{-\frac{2}{3}\sqrt{m}[2(E_g-\varepsilon_0)]^{3/2}/F(t')\}$ versus harmonic order. (c) Propagation effects $\alpha^2 \propto \exp[-2(t-t')/T_2]/(t-t')$ versus harmonic order. (d) Magnitude squared of the dipole moment as a function of harmonic order (blue); the product of the three preexponential terms in Eq. (34) represented by blue lines in (b)–(d) is plotted for the short- (red dots) and long- (green squares) trajectory branches; the magnitude is adapted to match the dipole moment. In (a)–(c) the shaded regions indicate the contributions from long trajectories.

B. Tomographic reconstruction of the impurity ground state

Figure 3(a) shows the generated harmonics versus birth (red line) and recombination (blue line) times from the semiclassical trajectories obtained from numerical solution of Eq. (33). There are two sets of solutions per optical cycle, a short trajectory and a long trajectory. The long-trajectory contributions are indicated by the shaded regions in Fig. 3. Figures 3(b)–3(d) examine the behavior of each of the preexponential terms in Eq. (34). Figures 3(b) and 3(c) present the ionization rate and propagation term, respectively. For ionization we have used the dominant atomic tunneling exponent [3,33]. Figure 3(d) shows $|d_0(\omega)|^2$ obtained from the diagonalization of the Hamiltonian (blue line), where k has been replaced with ω by virtue of relation (33c). We find that $|d_0(\omega)|^2$ decreases by about six orders of magnitude with increasing harmonic order. The rapid drop comes from the fact that the ground state extends over many unit cells and therewith populates only a small fraction of the BZ. In Fig. 3(d) we also plot the product of all three terms, where long and short trajectories are indicated by red dots and green squares, respectively. The short trajectories are dominant, and a comparison with $|d_0(\omega)|^2$ shows that the dipole moment determines the form of the harmonic spectrum over most of its range; this is confirmed in Fig. 4.

In Fig. 4 the harmonic intensity $|\tilde{j}|^2$ (blue line) is plotted, including both the impurity and intraband contributions. We note that the harmonics above the impurity ionization potential are dominated by the impurity term (see the Appendix). The strength of the above impurity gap harmonics drops rapidly until around the cutoff near the 71st harmonic. This behavior is consistent with the decrease of $|d_0(\omega)|^2$ (red dashed line), indicating that, of the three preexponential terms in Eq. (34), the dipole has the strongest influence on the shape of the harmonic spectrum. Consequently, using relation (33c) to connect harmonic order and k, we can reconstruct $d_0(k)$ from the magnitude of the harmonic spectrum. This is feasible, as the atomlike dipole moment is purely real or imaginary. For a complex dipole moment the phase of the harmonics must be considered, as in Ref. [44].

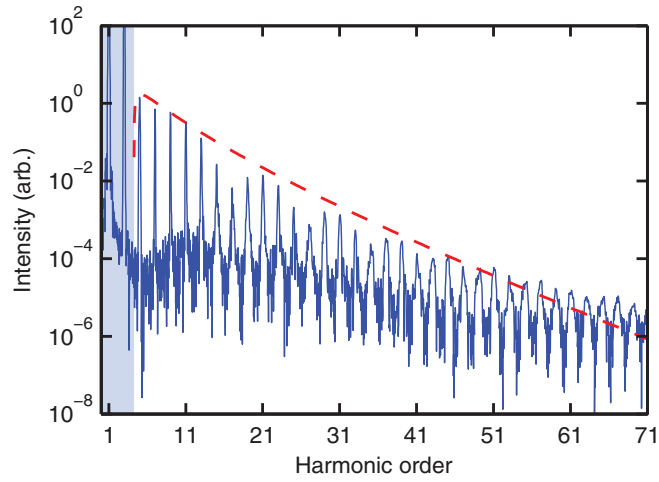

FIG. 4. Scaling comparison of the harmonic spectrum (blue solid line) to the dipole (red dashed line); the dipole has been shifted down in order to compare it with the spectrum. The harmonics in the shaded region are the ones whose energy is below $E_g - \varepsilon_0$.

To reconstruct the impurity ground state we take the inverse Fourier transform of $d_0(k)$ and divide it by x to obtain $B_0(x)$. In a three-dimensional experiment one would rotate the crystal and reconstruct the total wave function from 1D snapshots. Figure 5 shows the results of the tomographic reconstruction. The reconstructed wave function (red line)

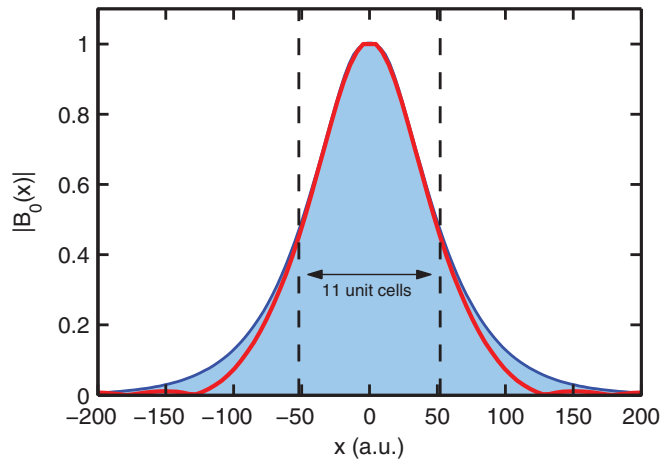

FIG. 5. Comparison between the impurity ground state (blue shaded area) and the reconstructed ground state (red line). The region between the vertical dashed lines represents 11 unit cells.

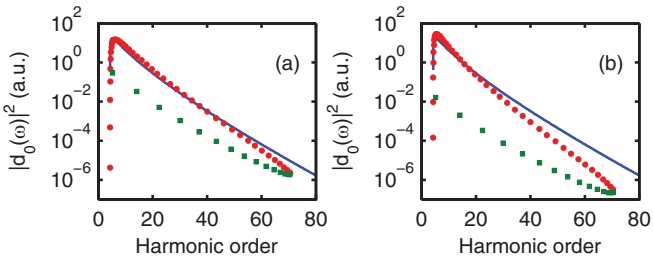

FIG. 6. Magnitude squared of the dipole moment as a function of harmonic order (blue line); the product of the three preexponential terms in Eq. (10) is plotted for the short- (red dots) and long- (green squares) trajectory branches for (a) the one-dimensional system and (b) a three-dimensional system. The magnitude of the semiclassical curves is adapted to match the dipole moment.

matches the impurity ground state well throughout the central region but deviates from the true wave function at the tails. This agrees with the fact that the difference between harmonic intensity and dipole scaling in Fig. 4 is biggest for small crystal momenta corresponding to slow wave function variations in real space. Further, the small oscillations in the harmonic spectrum in Fig. 4 do not appear to cause a substantial error in the reconstruction; they result from interference between harmonics generated in positive and negative half cycles as a consequence of the phase term in Eq. (34).

C. Dimensionality considerations for tomographic reconstruction

In our semiclassical model the ionization rate $w(t')$ and the propagation term that accounts for quantum spreading and dephasing $\alpha(t',t)$ are given by

$$w(t') \propto e^{-\frac{2}{3}\sqrt{m}(2E_0)^{3/2}/F(t')}, \tag{37a}$$

$$\alpha(t',t)^2 \propto \frac{e^{-2(t-t')/T_2}}{(t-t')^D}, \tag{37b}$$

where $E_0 = E_g - \varepsilon_0$ is the impurity ionization potential, $D \in \{1,2,3\}$ is the dimension, and t' and t are the birth and recombination times, respectively. The effective mass along the direction longitudinal to the laser polarization is given by m. In Eq. (37b) the term $(t-t')^{-D}$ accounts for the quantum spreading, and the term $e^{-2(t-t')/T_2}$ accounts for the effect of dephasing. Both terms have the strongest effect on the long trajectories as $(t-t')$ will be greatest for this trajectory branch.

The exponential scaling of the ionization rate depends on only the longitudinal components of the system along the direction of laser polarization; the transverse components appear only in the preexponential factor. As such, the dimensionality of the system is not expected to have a significant effect on the form of the ionization rate. Contrastingly, the quantum diffusion contribution $(t-t')^{-D}$ to the propagation term in Eq. (37b) will exhibit greater spreading for a three-dimensional system as opposed to a one-dimensional system.

Figure 6 shows the effect the dimension will have on the product $w(t')|d_0(k(t',t))|^2\alpha(t',t)^2$ in Eq. (34). Figure 6(a) shows this product for the one-dimensional system; this is a reproduction of Fig. 3(d). Figure 6(b) shows the product with $D=3$. The three-dimensional plot displays two main differences from the one-dimensional case. First, the separation between the long- and short-trajectory branches is greater in three dimensions than in one dimension. This occurs because spreading can occur in all three directions in the three-dimensional case. Second, because the spreading term is more pronounced in three dimensions, the semiclassical curve deviates more from the behavior of the dipole. This suggests that, for three-dimensional systems, it may be necessary to account for quantum diffusion before reconstructing the wave function. Accounting for quantum diffusion should be achievable in a straightforward manner using Eq. (34). For each birth and recombination time pair, $\alpha(t',t)$ can be calculated. This (t',t) pair corresponds to a particular harmonic, and thus, we have the mapping $\alpha(t',t) \to \alpha(\omega)$. The $\alpha(\omega)$ term can then be factored out of the harmonic spectrum, removing the effect of quantum diffusion for harmonic with frequency ω.

A more sophisticated reconstruction scheme could also remove the effects stemming from ionization. As a result of the complexity in calculating ionization rates in solids [45–49], the ionization rate could be measured by transient absorption spectroscopy [50] and then factored out of the harmonic spectrum in a manner similar to that described for removing the effects of quantum diffusion. Furthermore, the dipole moment extracted from Eq. (34) or from numerical analysis can be improved by using optimization techniques similar to the one used recently for all-optical band gap measurements [51]. Finally, for noncentrosymmetric materials the phase of the dipole is also important [52], facilitating the need for the phase of the harmonics to be measured for proper reconstruction.

IV. CONCLUSION

Here we have presented the microscopic theoretical underpinning for exploring strong-field physics in impurities. Our work makes a first step toward adapting technology developed for atomic and molecular gases to solid-state impurities. In contrast to gases, absorption will limit the material depth from which photons and electrons can be detected; as a result, propagation effects are expected to be less significant. Whether experimental tomographic reconstruction is as straightforward as found here remains to be seen. How dominant the dipole moment is in determining harmonic spectra will depend on various factors, such as dephasing time, material dimension, and parameters. Further, it has been demonstrated that for HHG to be viable, coherent buildup due to phase matching and field propagation effects should be considered [53]. To study these effects it would be necessary to couple the present theory to Maxwell's equations. That is beyond the scope of the current work and will be considered in a follow-up work.

Finally, it needs to be mentioned that our theoretical approach has been developed for shallow impurities. Deep impurities are more complex, as their wave function changes substantially over a unit cell. This results in a strong mixing between impurity and surrounding lattice wave function components. The resulting many-body effects, such as coupling to quasiparticles, need to be addressed with more sophisticated

theoretical approaches [29]. They will dominantly enter in the dipole moment and therewith in recombination; ionization will be influenced to a lesser extent, as the dipole moment enters in the preexponent. Propagation will be altered only close to the impurity, where the impurity potential yields higher-order corrections to the strong-field approximation. As a result, our simple approach will present a reasonable starting point to develop strong-field impurity physics in this more complex limit.

ACKNOWLEDGMENTS

All authors acknowledge support from the National Sciences and Engineering Research Council of Canada (NSERC). P.B.C. also acknowledges supported from the U.S. Air Force Office of Scientific Research (AFOSR) under Awards No. FA9550-16-1-0109 and No. FA9550-15-1-0037 and Canada's National Research Council (NRC).

APPENDIX: IMPURITY VERSUS INTRABAND HARMONICS

The HHG spectrum in Fig. 4 of the main text contains contributions from both the intraband and impurity terms. Figure 7 compares the individual contributions of each of these terms. The individual harmonic spectra are calculated by taking the absolute value squared of the Fourier transform of Eqs. (30) and (31). The harmonics generated by the impurity term are represented by the blue line, and those generated by the intraband current are represented by the green line. In the above-band-gap range, harmonics with $n \geqslant 5$, the spectrum is dominated by the impurity term by approximately three to six orders of magnitude, depending on the harmonic. The only exception is harmonic 5, where the impurity and intraband terms are comparable. In the below-band-gap regions, the intraband harmonics are the dominant signal. The red dashed line in Fig. 7 represents the dipole moment, which scales similarly to the impurity harmonic signal.

We note here that the density of impurities will have an effect on the intensities of the impurity and intraband harmonics. In our one-dimensional calculations we have an impurity density of approximately 10^{-3} impurities per lattice site. In three dimensions this density would be approximately

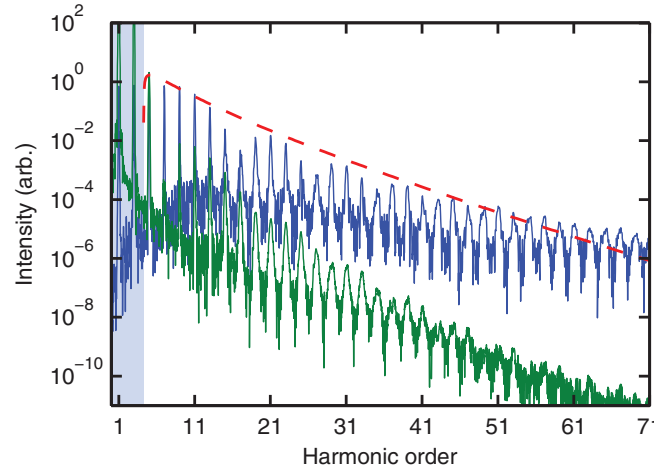

FIG. 7. The impurity (blue solid line) and intraband (green solid line) harmonic spectra. The red dashed line represents the dipole moment. The shaded area indicates the below-impurity ionization potential region. The dipole has been shifted on the y axis to compare with the shape of the harmonic spectra.

10^{-9} and will likely result in a decrease of impurity harmonics relative to the intraband spectrum. In our one-dimensional calculations the impurity harmonics range from three to six orders of magnitude above the intraband harmonics. As a result, a relative impurity density of around 10^{-6} corresponding to an impurity density of approximately $10^{16}\,\mathrm{cm}^{-3}$ should be sufficient to still observe stronger impurity harmonics.

Further, there is another parameter that determines the strength of impurity versus intraband HHG, which is the laser intensity. For the intraband harmonics to develop, the electron must explore a significant portion of the nonlinear part of the band. Due to the low field intensities used here, the electron explores only about a third of the Brillouin zone and does not experience the full nonlinear portion of the conduction band, resulting in a reduction of the intensity of intraband harmonics. When the electron explores only a limited region of the Brillouin zone near the Γ point, the intensity of the intraband harmonics decreases with harmonic order at a rate much larger than the impurity harmonics. The above discussion highlights the need for careful consideration when determining doping rates and laser parameters.

[1] P. B. Corkum, Plasma Perspective on Strong Field Multiphoton Ionization, Phys. Rev. Lett. **71**, 1994 (1993).
[2] P. B. Corkum and F. Krausz, Attosecond science, Nat. Phys. **3**, 381 (2007).
[3] M. Lewenstein, P. Balcou, M. Y. Ivanov, A. L'Huillier, and P. B. Corkum, Theory of high-harmonic generation by low-frequency laser fields, Phys. Rev. A **49**, 2117 (1994).
[4] X. M. Tong, Z. X. Zhao, and C. D. Lin, Theory of molecular tunneling ionization, Phys. Rev. A **66**, 033402 (2002).
[5] H. Akagi, T. Otobe, A. Staudte, A. Shiner, F. Turner, R. Dörner, D. M. Villeneuve, and P. B. Corkum, Laser tunnel ionization from multiple orbitals in HCl, Science **325**, 1364 (2009).
[6] J. Itatani, J. Levesque, D. Zeidler, H. Niikura, H. Pépin, J. C. Kieffer, P. B. Corkum, and D. M. Villeneuve, Tomographic imaging of molecular orbitals, Nature (London) **432**, 867 (2004).
[7] S. Baker, J. S. Robinson, C. A. Haworth, H. Teng, R. A. Smith, C. C. Chirila, M. Lein, J. W. G. Tisch, and J. P. Marangos, Probing proton dynamics in molecules on an attosecond time scale, Science **312**, 424 (2006).
[8] H. J. Wörner, J. B. Bertrand, D. V. Kartashov, P. B. Corkum, and D. M. Villeneuve, Following a chemical reaction using high-harmonic interferometry, Nature (London) **466**, 604 (2010).
[9] D. Shafir, Y. Mairesse, D. Villeneuve, P. B. Corkum, and N. Dudovich, Atomic wavefunctions probed through strong-field light-matter interaction, Nat. Phys. **5**, 412 (2009).
[10] S. Patchkovskii, Z. Zhao, T. Brabec, and D. M. Villeneuve, High Harmonic Generation and Molecular Orbital Tomography

in Multielectron Systems: Beyond the Single Active Electron Approximation, Phys. Rev. Lett. **97**, 123003 (2006).

[11] C. Vozzi, M. Negro, F. Calegari, G. Sansone, M. Nisoli, S. De Silvestri, and S. Stagira, Generalized molecular orbital tomography, Nat. Phys. **7**, 822 (2011).

[12] C. D. Lin, A.-T. Le, Z. Chen, T. Morishita, and R. Lucchese, Strong-field rescattering physics—Self-imaging of a molecule by its own electrons, J. Phys. B **43**, 122001 (2010).

[13] B. Wolter, M. G. Pullen, A.-T. Le, M. Baudisch, K. Doblhoff-Dier, A. Senftleben, M. Hemmer, C. D. Schröter, J. Ullrich, T. Pfeifer, R. Moshammer, S. Gräfe, O. Vendrell, C. D. Lin, and J. Biegert, Ultrafast electron diffraction imaging of bond breaking in di-ionized acetelyne, Science **354**, 308 (2016).

[14] D. N. Fittinghoff, P. R. Bolton, B. Chang, and K. C. Kulander, Observation of Nonsequential Double Ionization of Helium with Optical Tunneling, Phys. Rev. Lett. **69**, 2642 (1992).

[15] M. B. Gaarde, K. J. Schafer, K. C. Kulander, B. Sheehy, D. Kim, and L. F. DiMauro, Strong Species Dependence of High Order Photoelectron Production in Alkali Metal Atoms, Phys. Rev. Lett. **84**, 2822 (2000).

[16] B. Walker, B. Sheehy, K. C. Kulander, and L. F. DiMauro, Elastic Rescattering in the Strong Field Tunneling Limit, Phys. Rev. Lett. **77**, 5031 (1996).

[17] S. Ghimire, A. D. DiChiara, E. Sistrunk, P. Agostini, L. F. DiMauro, and D. A. Reis, Observation of high-order harmonic generation in a bulk crystal, Nat. Phys. **7**, 138 (2011).

[18] T. T. Luu, M. Garg, S. Yu. Kruchinin, A. Moulet, M. Th. Hassan, and E. Goulielmakis, Extreme ultraviolet high-harmonic spectroscopy of solids, Nature (London) **521**, 498 (2015).

[19] G. Vampa, T. J. Hammond, N. Thiré, B. E. Schmidt, F. Légaré, C. R. McDonald, T. Brabec, and P. B. Corkum, Linking high harmonic generation from gases and solids, Nature (London) **522**, 462 (2015).

[20] G. Ndabashimiye, S. Ghimire, M. Wu, D. A. Browne, K. J. Schafer, M. B. Gaarde, and D. A. Reis, Solid-state harmonics beyond the atomic limit, Nature (London) **534**, 520 (2016).

[21] B. Zaks, R. B. Liu, and M. S. Sherwin, Experimental observation of electron-hole recollisions, Nature (London) **483**, 580 (2012).

[22] O. Schubert *et al.*, Sub-cycle control of terahertz high-harmonic generation by dynamical Bloch oscillations, Nat. Photonics **8**, 119 (2014).

[23] M. Hohenleutner *et al.*, Real time observation of interfering crystal electrons in high-harmonic generation, Nature (London) **523**, 572 (2015).

[24] D. Golde, T. Meier, and S. W. Koch, High harmonics generated in semiconductor nanostructures by the coupled dynamics of optical inter- and intraband excitations, Phys. Rev. B **77**, 075330 (2008).

[25] G. Vampa, C. R. McDonald, G. Orlando, D. D. Klug, P. B. Corkum, and T. Brabec, Theoretical Analysis of High-Harmonic Generation in Solids, Phys. Rev. Lett. **113**, 073901 (2014).

[26] G. Vampa, C. R. McDonald, G. Orlando, P. B. Corkum, and T. Brabec, Semiclassical analysis of high harmonic generation in bulk crystals, Phys. Rev. B **91**, 064302 (2015).

[27] M. Sivis, M. Taucer, G. Vampa, K. Johnston, A. Staudte, A. Yu. Naumov, D. M. Villeneuve, C. Ropers, and P. B. Corkum, Tailored semiconductors for high-harmonic optoelectronics, Science **357**, 303 (2017).

[28] T. Huang, X. Zhu, L. Li, X. Liu, P. Lan, and P. Lu, High-order-harmonic generation of a doped semiconductor, Phys. Rev. A **96**, 043425 (2017).

[29] P. M. Koenraad and M. E. Fratté, Single dopants in semiconductors, Nat. Mater. **10**, 91 (2011).

[30] E. N. Adams II, Motion of an electron in a perturbed periodic potential, Phys. Rev. **85**, 41 (1952).

[31] J. M. Luttinger and W. Kohn, Motion of electrons and holes in perturbed periodic fields, Phys. Rev. **97**, 869 (1955).

[32] W. Kohn and J. M. Luttinger, Hyperfine splitting of donor states in silicon, Phys. Rev. **97**, 883 (1955).

[33] L. V. Keldysh, Ionization in the field of a strong electromagnetic wave, Sov. Phys. JETP **20**, 1307 (1965).

[34] S. T. Pantelides, The electronic structure of impurities and other point defects in semiconductors, Rev. Mod. Phys. **50**, 797 (1978).

[35] P. Y. Yu and M. Cardona, *Fundamentals of Semicondcutors* (Springer, Berlin, 2001).

[36] N. W. Ashcroft and N. D. Mermin, *Solid State Physics* (Saunders College, Philadelphia, 1976).

[37] C. R. McDonald, K. S. Amin, S. Aalmalki, and T. Brabec, Enhancing High Harmonic Output in Solids through Quantum Confinement, Phys. Rev. Lett. **119**, 183902 (2017).

[38] T. Luo, J. Garg, J. Shiomi, K. Esfarjani, and G. Chen, Gallium arsenide thermal conductivity and optical phonon relaxation times from first-principles calculations, Europhys. Lett. **101**, 16001 (2013).

[39] Y. Shinohara K. Yabana, Y. Kawashita, J.-I. Iwata, T. Otobe, and G. F. Bertsch, Coherent phonon generation in time-dependent density functional theory, Phys. Rev. B **82**, 155110 (2010).

[40] M. Hase, M. Katsuragawa, A. M. Constantinescu, and H. Petek, Frequency comb generation at terahertz frequencies by coherent phonon excitation in silicon, Nat. Photonics **6**, 243 (2012).

[41] B. K. Meyer, J. Sann, D. M. Hofmann, C. Neumann, and A. Zeuner, Shallow donors and acceptors in ZnO, Semicond. Sci. Technol. **20**, S62 (2005).

[42] M. C. Hoffmann and J. A. Fülöp, Intense ultrashort terahertz pulses: generation and applications, J. Phys. D **44**, 083001 (2011).

[43] M. J. Caldas, A. Fazzio, and A. Zunger, A universal trend in the binding energies of deep impurities in semiconductors, Appl. Phys. Lett. **45**, 671 (1984).

[44] W. Boutu, S. Haessler, H. Merdji, P. Breger, G. Waters, M. Stankiewicz, L. J. Frasinski, R. Taieb, J. Caillat, A. Maquet, P. Monchicourt, B. Carre, and P. Salieres, Coherent control of attosecond emission from aligned molecules, Nat. Phys. **4**, 545 (2008).

[45] V. E. Gruzdev, Photo-ionization rate in wide bandgap crystals, Phys. Rev. B **75**, 205106 (2007).

[46] P. A. Zhokhov and A. M. Zheltikov, Field-Cycle Resolved Photoionization in Solids, Phys. Rev. Lett. **113**, 133903 (2014).

[47] C. R. McDonald, G. Vampa, P. B. Corkum, and T. Brabec, Intense-Laser Solid State Physics: Unraveling the Difference Between Semiconductors and Dielectrics, Phys. Rev. Lett. **118**, 173601 (2017).

[48] P. A. Zhokhov and A. M. Zheltikov, Depth-resolved subcycle dynamics of photoionization in solids, Phys. Rev. A **96**, 033415 (2017).

[49] V. Gruzdev and O. Sergaeva, Ultrafast modification of band structure of wide-band-gap solids by ultrashort pulses of laser-driven electron oscillations, Phys. Rev. B **98**, 115202 (2018).

[50] M. Schultze, K. Ramasesha, C. D. Pemmaraju, S. A. Sato, D. Whitmore, A. Gandman, J. S. Prell, L. J. Borja, D. Prendergast, K. Yabana, D. M. Neumark, and S. R. Leone, Attosecond bandgap dynamics in silicon, Science **346**, 1348 (2014).

[51] G. Vampa, T. J. Hammond, N. Thiré, B. E. Schmidt, F. Legaré, C. R. McDonald, T. Brabec, D. D. Klug, and P. B. Corkum, All-Optical Reconstruction of Crystal Bandstructure, Phys. Rev. Lett. **115**, 193603 (2015).

[52] S. Jiang, J. Chen, H. Wei, C. Yu, R. Lu, and C. D. Lin, Role of the Transition Dipole Amplitude and Phase on the Generation of Odd and Even High-Order Harmonics in Crystals, Phys. Rev. Lett. **120**, 253201 (2018).

[53] I. Floss, C. Lemell, G. Wachter, V. Smejkal, S. A. Sato, X. Tong, K. Yabana, and J. Burgdörfer, *Ab initio* multiscale simulation of high-order harmonic generation in solids, Phys. Rev. A **97**, 011401(R) (2018).